

Adaptive Multi-Scale Integration Unlocks Robust Cell Annotation in Histopathology Images

Yinuo Xu^{1,3} Yan Cui^{2,3} Mingyao Li^{4,*} Zhi Huang^{3,4,*}

¹Department of Computer and Information Science, University of Pennsylvania

²Department of Bioengineering, University of Pennsylvania

³Department of Pathology and Laboratory Medicine, University of Pennsylvania

⁴Department of Biostatistics, Epidemiology and Informatics, University of Pennsylvania

xuyinuo@cis.upenn.edu, yan12@seas.upenn.edu,

mingyao@penmedicine.upenn.edu, zhi.huang@penmedicine.upenn.edu

* To whom the correspondence should be addressed: Zhi Huang, Mingyao Li

Abstract

*Identifying cell types and subtypes in routine histopathology is fundamental for understanding disease. Existing tile-based models captures nuclear detail but miss the broader tissue context that influences cell identity. Current human annotations are coarse-grained and uneven across studies, making fine-grained, subtype-level classification difficult. In this study, we build a marker-guided dataset from Xenium spatial transcriptomics with single-cell-resolution labels for more than two million cells across eight organs and 16 classes to overcome the lack of high-quality annotations. Leveraging this data resource, we introduce **NuClass**, a pathologist workflow-inspired framework for cell-wise multi-scale integration of nuclear morphology and microenvironmental context. It combines **Path local**, which focuses on nuclear morphology from 224^2 -pixel crops, and **Path global**, which models the surrounding 1024^2 -pixel neighborhood, through a learnable gating module to balance local and global details. An uncertainty-guided objective directs the global path to prioritize regions where the local path is uncertain, and we provide calibrated confidence estimates and Grad-CAM maps for interpretability. Evaluated on three fully held-out cohorts, NuClass achieves up to **96% F1** for its best-performing class, outperforming strong baselines. Our results demonstrate that multi-scale, uncertainty-aware fusion can bridge the gap between slide-level pathological foundation models and reliable, cell-level phenotype prediction.*

1. Introduction

Understanding cell types and their spatial interplay within tissues is central to studying human disease. While emerg-

ing technologies such as spatial transcriptomics enable cell type identification through marker genes, hematoxylin and eosin (H&E)-stained whole-slide images remain the most practical and widely adopted modality in routine clinical workflows, serving as the cornerstone for differential diagnosis and quantitative evaluation and guiding assessment of cancer stage, transplant outcomes, and treatment strategies.

In H&E images, nuclei segmentation [43] is well studied, but assigning detected nuclei to robust, generalizable cell identities—i.e., cell classification—remains challenging. This largely stems from (1) the lack of large-scale, cross-slice, high-quality, unified training datasets and (2) the difficulty of learning cell type-specific features under heterogeneous morphology across patients, organs, and scanners. Together, these issues reflect two core limitations: *data scarcity* and *model design*.

On the data side, recent studies show that a lack of *high-quality, cell-level annotated training data*, combined with stain/tissue heterogeneity and domain shifts, strongly constrains deep models for cell classification. Human annotations are often coarse and inconsistent and require substantial expert effort, limiting subcellular precision, scalability, and the diversity of labeled cell types.

On the modeling side, three challenges remain. (i) Current cell embedding models are largely unaware of a cell’s neighborhood, even though distinguishing, for example, cancer-associated from normal epithelial cells or macrophages from T cells often requires context beyond the local nuclear image. Multi-scale pipelines for gigapixel slides improve slide-level reasoning [7], but aggregation typically occurs at the bag or slide level, leaving the instance-wise balance between morphology and context underexplored. (ii) Models struggle with varying annotation granularities and taxonomies across tissues and datasets

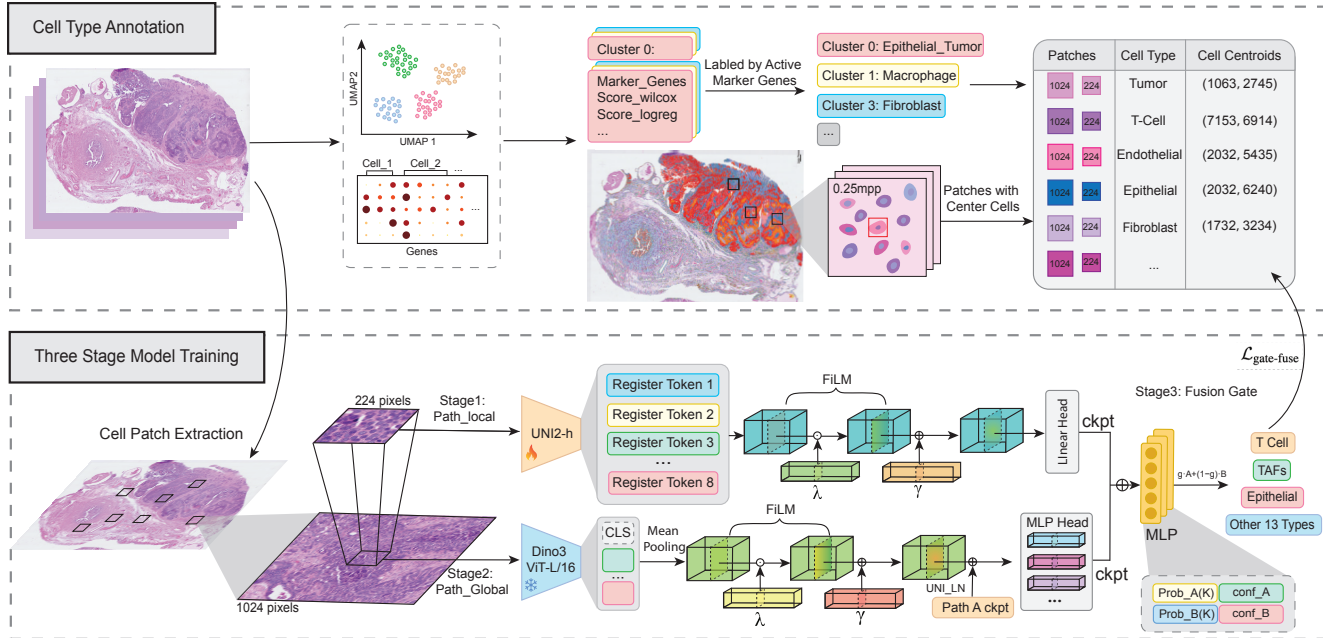


Figure 1. **NuClass: cell-wise multi-scale classification with gating.** (Top) From whole-slide images (WSIs), we extract paired fields centered on each cell: a nucleus-scale crop (224^2 at 0.25 mpp) and a co-registered contextual field-of-view (FOV; default 1024^2 at 0.25 mpp). Spatial assays (Xenium-like) provide gene-marker profiles and cell centroids, enabling scalable, subcellular annotations. (Stage 1, Path local) A UNi2-h morphology backbone processes the 224^2 crop. A tissue-conditioned FiLM modulates features before a linear head outputs per-cell probabilities. (Stage 2, Path global) A DINOv3 ViT-L/16 encoder ingests the 1024^2 contextual FOV; its representation is concatenated with a Path local morphology vector to predict complementary probabilities. (Stage 3, Fusion Gate) A lightweight *cell-wise gate* receives statistics from both distributions and compact feature projections, then fuses experts in *probability space* $\mathbf{p}_{\text{mix}} = (1 - g)\mathbf{p}_{\text{local}} + g\mathbf{p}_{\text{global}}$. The gate learns *which expert to trust per cell*, not to average logits.

(e.g., the same cell may be labeled as “inflammatory cell,” “immune cell,” or “lymphocyte”). (iii) There is no large-scale pretrained foundation model across diverse diseases and organs to provide a strong encoder for downstream fine-tuning.

These spatial and semantic nuances across data, annotations, and models remain underexplored, creating an urgent need for a foundation model trained on millions of cells that can harmonize diverse annotations and enable deeper understanding of cell types and tissue organization.

To address data scarcity and model design jointly, we present a workflow from data curation to model development to advance understanding of cellular and nuclear features in H&E-stained images. On the data side, we build a scalable, *marker-guided* annotation pipeline on Xenium spatial assays that assigns fine-grained cell types with pixel-level coordinates to millions of cells, complementing and refining human supervision [1]. The resulting labels are objective and reproducible across tissues and institutions and provide precise anchors for cross-scale modeling and evaluation (Fig. 1, top).

On the modeling side, we develop **NuClass**, an adaptive framework for *cell-wise* multi-scale integrated learning. NuClass uses two fixed fields of view: **Path local** fo-

cuses on nucleus-centered morphology using small crops, whereas **Path global** processes the co-registered larger neighborhood to capture tissue architecture and micro-environmental cues. A learnable gate decides, for each cell, how much to rely on local detail versus global context, and training encourages the two paths to specialize and complement rather than duplicate one another.

At scale, NuClass generalizes across organs and datasets for reliable cell-level phenotyping. Trained on more than 2M marker-labeled cells spanning 16 types across 8 organs and evaluated on three fully held-out cohorts (about 0.28M cells), it achieves up to **96%** for its best-performing cell class and consistently matches or surpasses strong baselines while producing well-calibrated, interpretable predictions.

2. Related Work

Multi-organ multi-class H&E cell datasets. Recent dataset efforts have shifted from single-organ toward multi-organ collections, such as MoNuSAC [41] (4 tissues) and PanNuke [13] (19 organs/tissues). However, due to the scarcity of large, well-annotated cell datasets, most cell-classification models remain tailored to specific organs or narrow use-cases, as in HoVer-Net [16] and CellViT [21].

Foundation models for cell classification. Foundation models are reshaping computational pathology by learning general-purpose visual or vision–language representations from large, heterogeneous datasets [8, 11, 27, 28, 42, 44, 45]. These approaches transfer well on patch- and slide-level benchmarks, and vision–language systems extend to retrieval, question answering, and outcome prediction. Yet most progress still targets slide-level endpoints. In routine practice, a cell’s identity depends on both its nuclear morphology and the tissue neighborhood in which it resides, but existing systems seldom integrate these two sources of evidence at *per-cell* granularity. The recent VOLTA algorithm [30] leverages over 800k cells across six cancer types to train a self-supervised cell representation model via contrastive learning, but it still relies on cell patches and spatial neighborhoods as unlabeled training signals and does not provide label-consistent, cross-organ cell types.

Per-cell representation learning at scale. The transition from patch-level to cell-level understanding marks a fundamental step toward morphological precision. Traditional architectures like HoVer-Net [16] and CellViT [19] jointly segment and classify cells, yet remain trained on a limited set of annotated organs. Graph- or structure-aware models [26] extend this by modeling cell neighborhoods and propagating context among adjacent cells to capture micro-environmental cues. More recently, VOLTA [30] proposed environment-aware contrastive learning, jointly encoding nuclear morphology and tissue surroundings to obtain self-supervised embeddings over 0.8M cells; however, these embeddings remain unlabeled and cannot be directly aligned across organs or histologic types. Beyond isolated cells, cross-organ datasets such as PanNuke [13, 14], Lizard [17], and NuCLS [2] highlight the importance of organ diversity for robust per-cell modeling, yet per-cell recognition still struggles to unify morphology and context across domains. A scalable foundation model explicitly designed for per-cell representation—bridging nuclear texture, multi-scale tissue context, and cross-organ semantics—therefore remains an open problem in computational pathology.

3. Method

Given a cell–centric dataset with tissue annotations $\mathcal{D} = \{(\mathbf{x}_i^{224}, \mathbf{x}_i^{ctx}, t_i, y_i)\}_{i=1}^N$, $\mathbf{x}_i^{224} \in \mathbb{R}^{224 \times 224 \times 3}$ denotes a local 224^2 patch, $\mathbf{x}_i^{ctx} \in \mathbb{R}^{H \times W \times 3}$ ($H=W=1024$ by default) a wider contextual view, t_i the tissue type (e.g., liver/lung), and $y_i \in \{1, \dots, C\}$ the target cell class. We introduce two complementary branches: **Path local** focuses on *cell morphology* with tissue-aware adaptation, while **Path global** injects *context* to cover Path local’s blind spots. For fusion, we *freeze* the two branches and train a fusion gate to combine predictions in *probability space*, yielding stable gains without modifying either backbone.

Notation. For a C -class softmax output we write $\mathbf{p} \in$

Δ^{C-1} to mean that $\mathbf{p} = (p_1, \dots, p_C)^\top \in \mathbb{R}^C$ lies on the probability simplex $\Delta^{C-1} = \{\mathbf{u} \in \mathbb{R}^C : u_c \geq 0, \sum_c u_c = 1\}$. We denote by $p_{\max} = \max_c p_c$ the largest class probability (“confidence”), by $H(\mathbf{p}) = -\sum_{c=1}^C p_c \log p_c$ the Shannon entropy [36], and by $\text{margin}(\mathbf{p}) = p_{(1)} - p_{(2)}$ the gap between the largest and second-largest coordinates (a simple confidence margin). For an input example x_i , $\mathbf{p}_{\text{local}}$ and $\mathbf{p}_{\text{global}}$ are the softmax probability vectors predicted by Path local and Path global, respectively; \mathbf{p}_{mix} denotes the final fused distribution (a convex combination used at test time).

3.1. Path local: Tissue-aware Cell Morphology Classifier

Motivation and task. In high-throughput pathology, *morphology* is the most direct signal, path local aims to learn robust, transferable morphology from 224^2 patches by *adapting to tissue domains*.

Architecture. We adopt a UNI2-h ViT backbone \mathcal{F}_{uni} [8, 12] to extract a global feature $\mathbf{h}_i = \mathcal{F}_{\text{uni}}(\mathbf{x}_i^{224}) \in \mathbb{R}^{1536}$. LayerNorm [3] and FiLM [33] (conditioned on tissue) stylize the feature:

$$\mathbf{e}_t = \text{Emb}(t_i) \in \mathbb{R}^{d_t}, \quad (1)$$

$$(\gamma_i, \beta_i) = \phi(\mathbf{e}_t) \in \mathbb{R}^{1536} \times \mathbb{R}^{1536}, \quad (2)$$

$$\tilde{\mathbf{h}}_i = \text{LN}(\mathbf{h}_i) \odot (1 + \gamma_i) + \beta_i, \quad (3)$$

where $\phi(\cdot)$ is a 2-layer MLP and \odot denotes elementwise product. A 2-layer MLP head outputs logits and probabilities: $\mathbf{z}_i^{\text{local}} = \text{Head}_{\text{local}}(\tilde{\mathbf{h}}_i) \in \mathbb{R}^C$, $\mathbf{p}_{\text{local}} = \text{softmax}(\mathbf{z}_i^{\text{local}})$.

Loss and schedule. We use class-balanced cross-entropy with label smoothing [9, 29]:

$$\mathcal{L}_{\text{local}} = -w_{y_i} \sum_{c=1}^C q_{i,c} \log p_{\text{local},c}, \quad q_{i,c} = \begin{cases} 1 - \epsilon, & c = y_i, \\ \frac{\epsilon}{C-1}, & c \neq y_i, \end{cases} \quad (4)$$

with class weights from the *Effective Number*: $w_c \propto \frac{1-\beta}{1-\beta^{n_c}}$ (n_c : samples of class c). We adopt a *probe warm-up* followed by full fine-tuning [22], and apply layer-wise LR decay to the ViT for stability [4, 39].

Path local emphasizes *cell-intrinsic morphology*. Yet 224^2 local windows can be insufficient under complex micro-environments or cell–cell interactions, motivating Path global to supply *context*.

3.2. Path global: Context-aware Complementary Branch

Motivation and task. Many cell types become separable only when neighborhood cues (e.g., glands, vessels, immune infiltration) are visible; a 224^2 crop alone is often insufficient to tell them apart. Path global *injects wide-field*

context while preserving Path local’s morphology competence, and—crucially—learns *where Path local is weak* instead of relearning what Path local already solves.

Local-initialized backbone. Path global reuses the UNI2-h backbone from Path local on the 224² crop. We initialize UNI, the tissue-aware FiLM, and the local-style head from Path local’s checkpoint. For the first E_{freeze} epochs these modules are frozen, preventing early drift and ensuring Path global starts from Path local’s morphology.

Architecture (with tissue FiLM in context). Given a crop \mathbf{x}_i^{224} and a contextual view $\mathbf{x}_i^{\text{ctx}} \in \mathbb{R}^{H \times W \times 3}$, we build a two-stream encoder:

$$\mathbf{u}_i = \mathcal{F}_{\text{uni}}(\mathbf{x}_i^{224}) \in \mathbb{R}^{1536}, \quad (5)$$

$$\mathbf{v}_i = \mathcal{G}_{\text{ctx}}(\mathbf{x}_i^{\text{ctx}}) \in \mathbb{R}^{1024}, \quad (\text{DINOv3; token mean}) \quad [37] \quad (6)$$

apply tissue-conditioned FiLM to the context stream,

$$(\gamma_i^{\text{ctx}}, \beta_i^{\text{ctx}}) = \phi_{\text{ctx}}(\mathbf{e}_t), \quad (7)$$

$$\tilde{\mathbf{v}}_i = \text{LN}(\mathbf{v}_i) \odot (1 + \gamma_i^{\text{ctx}}) + \beta_i^{\text{ctx}}, \quad (8)$$

then project and concatenate:

$$\begin{aligned} \mathbf{u}'_i &= \text{LN}(\mathbf{u}_i) \mathbf{W}_u \in \mathbb{R}^{512}, \\ \mathbf{v}'_i &= \text{LN}(\tilde{\mathbf{v}}_i) \mathbf{W}_v \in \mathbb{R}^{512}, \\ \mathbf{s}_i &= [\mathbf{u}'_i; \mathbf{v}'_i] \in \mathbb{R}^{1024}, \end{aligned} \quad (9)$$

$$\mathbf{z}_i^{\text{global}} = \text{Head}_{\text{global}}(\mathbf{s}_i), \quad \mathbf{p}_i^{\text{global}} = \text{softmax}(\mathbf{z}_i^{\text{global}}). \quad (10)$$

Why this fusion is efficient. (i) Both streams are LayerNorm’ed and projected to a common 512-d space, so their scales are comparable; (ii) the 1024-d concatenation lets $\text{Head}_{\text{global}}$ learn the mixture *in feature space*, which is expressive yet compute-efficient; (iii) empirically this “LN+linear-to-512, then concat” is low-cost and consistently effective.

Context resolution and resampling. Unless specified otherwise, the context field-of-view (FOV) is a 1024² square centered at the target cell at native slide resolution. For compute efficiency we may *resample the same FOV* to $r_{\text{ctx}} \in \{512, 768, 1024\}$ (default $r_{\text{ctx}}=1024$) before DINO. Resampling preserves the spatial FOV—no cropping/padding—only the sampling *density* changes. If an integer ratio exists (e.g., 1024→512) we use stride decimation; otherwise bilinear interpolation. With patch size 16, DINO processes $S = (r_{\text{ctx}}/16)^2$ tokens and attention scales as $\mathcal{O}(S^2)$ [40]; we therefore employ *micro-batched* forward (e.g., 16–64) to bound memory and compilation latency without sacrificing throughput. For cells near slide boundaries, out-of-range regions are mirrored or reflected so that the effective FOV remains 1024² without introducing artificial padding or empty borders.

Local-aware weighting (definition). Let $\mathbf{z}_i^{\text{local}}$ be Path local head logits and $\mathbf{p}_i^{\text{local}} = \text{softmax}(\mathbf{z}_i^{\text{local}})$. We up-weight samples for which Path local is uncertain by

$$w_i = (1 - p_i^{\text{local}}(y_i))^\gamma \quad (11)$$

so w_i increases when Path local assigns a lower probability to the ground-truth class; this weighting mirrors the focal reweighting pattern [23].

Complementarity supervision (losses). Our default objective for Path global is

$$\mathcal{L}_{\text{main}} = \mathbb{E}_i [w_i \cdot \ell(\mathbf{z}_i^{\text{global}}, y_i)], \quad (12)$$

$$\mathcal{L}_{\text{stable}} = \mathbb{E}_i [\ell(\mathbf{z}_i^{\text{global}}, y_i)], \quad (13)$$

$$\mathcal{L}_{\text{PathGlobal}} = \mathcal{L}_{\text{main}} + \lambda_{\text{stable}} \mathcal{L}_{\text{stable}}, \quad (14)$$

where $\ell(\mathbf{z}, y) = -\sum_{c=1}^C w_c q_c(y) \log \text{softmax}(\mathbf{z})_c$ is class-balanced CE with label smoothing (Effective-Number weights w_c [9, 29]). Intuitively, $\mathcal{L}_{\text{main}}$ *up-weights* samples where Path local is unsure via Eq. (11), and $\mathcal{L}_{\text{stable}}$ prevents Path global from ignoring easy samples entirely. This simple default— $\mathcal{L} = \mathcal{L}_{\text{main}} + \lambda_{\text{stable}} \mathcal{L}_{\text{stable}}$ —worked robustly in all experiments.

Regularizers: “use context when helpful”. We apply two light regularizers to avoid collapse to the crop stream: (i) **Context dropout** ($\mathbf{v}'_i \leftarrow \mathbf{0}$ with prob. ρ), encouraging Path global to use context only when present; (ii) **Context warm-up**, concatenating $[\mathbf{u}'_i; \alpha \mathbf{v}'_i]$ with α ramped from α_0 to 1 over the first E_α epochs. These follow dropout/stochastic depth and curriculum learning [5, 20, 38].

Why it yields complementarity. Eq. (11) shifts gradient mass to the *Path local-hard* region (small $p_i^{\text{local}}(y_i)$), while Eq. (13) keeps Path global calibrated on easy cases. Starting from a Path local–initialized (and briefly frozen) morphology backbone avoids early drift; warm-up/dropout ensure Path global exploits context only when it helps. Together, Path global learns *contextual evidence Path local lacks* rather than duplicating morphology decisions.

3.3. Gated Fusion of Path local and Path global

Motivation and formulation. Path local and Path global exploit different signals—fine nuclear morphology vs. wide-field context—and their logits can reside on different scales with distinct uncertainty profiles. Mixing logits is brittle. We therefore fuse in *probability space* via a scalar, per-cell gate $g_i \in [0, 1]$ (mixture-of-experts):

$$\mathbf{p}_{\text{mix},i} = (1 - g_i) \mathbf{p}_{\text{local},i} + g_i \mathbf{p}_{\text{global},i}, \quad (15)$$

which is numerically stable and cannot overshoot either path.

Gate inputs and architecture (GT-free). The gate reads two compact feature projections and GT-free distributional

statistics. Let $\mathbf{f}_i^{\text{local}} \in \mathbb{R}^{1536}$ be Path local’s pre-head feature and $\mathbf{s}_i^{\text{global}} \in \mathbb{R}^{1024}$ be Path global’s fused feature (UNI patch + DINO context). We form

$$\begin{aligned}\tilde{\mathbf{f}}_i^{\text{local}} &= \text{LN}(\mathbf{f}_i^{\text{local}}) \mathbf{W}^{\text{local}} \in \mathbb{R}^{d_{\text{local}}}, \\ \tilde{\mathbf{s}}_i^{\text{global}} &= \text{LN}(\mathbf{s}_i^{\text{global}}) \mathbf{W}^{\text{global}} \in \mathbb{R}^{d_{\text{global}}}.\end{aligned}\quad (16)$$

We then assemble a statistic vector

$$\begin{aligned}r_i &= [p_{\max}^{\text{local}}, p_{\max}^{\text{global}}, \bar{H}(\mathbf{p}_{\text{local}}), \bar{H}(\mathbf{p}_{\text{global}}), \\ &\quad \text{margin}(\mathbf{p}_{\text{local}}), \text{margin}(\mathbf{p}_{\text{global}}), \rho_i, |\rho_i|],\end{aligned}\quad (17)$$

where $p_{\max}^{\text{local}} = \max_c p_c^{\text{local}}$ is top-1 confidence, $\bar{H}(\cdot)$ is entropy normalized by $\log C$, $\text{margin}(\cdot) = p_{(1)} - p_{(2)}$, and

$$\rho_i \triangleq p_{\max}^{\text{global}} - p_{\max}^{\text{local}}$$

captures GT-free confidence disagreement between the two paths. A two-layer MLP $\psi(\cdot)$ outputs

$$g_i = \sigma(\psi([\tilde{\mathbf{f}}_i^{\text{local}}; \tilde{\mathbf{s}}_i^{\text{global}}; r_i])).\quad (18)$$

Supervision: “choose whom to trust” (training-only use of GT). To supervise the gate, we define predicted labels $\hat{y}_{\text{local}} = \arg \max_c p_{i,c}^{\text{local}}$, $\hat{y}_{\text{global}} = \arg \max_c p_{i,c}^{\text{global}}$ and a *soft* preference using the ground-truth class:

$$\begin{aligned}\Delta_i^{(y)} &\triangleq p_i^{\text{global}}(y_i) - p_i^{\text{local}}(y_i), \\ \tilde{g}_i &= \begin{cases} 1, & \hat{y}_{\text{global}}=y_i \wedge \hat{y}_{\text{local}} \neq y_i, \\ 0, & \hat{y}_{\text{local}}=y_i \wedge \hat{y}_{\text{global}} \neq y_i, \\ \sigma(\kappa \Delta_i^{(y)}), & \text{otherwise.} \end{cases}\end{aligned}$$

Crucially, $\Delta_i^{(y)}$ is used only for supervision and loss weighting during training; it is never part of the gate input r_i and is not needed at test time.

Conflict-aware weighting (training-only). We emphasize samples on which the two paths disagree, and modulate by their confidence gap on the ground-truth class:

$$w_i = 1 + \lambda_{\text{conf}} \cdot \mathbf{1}[(\hat{y}_{\text{local}}=y_i) \oplus (\hat{y}_{\text{global}}=y_i)] + \lambda_{\Delta} |\Delta_i^{(y)}|^{\gamma_{\Delta}}.\quad (19)$$

Objective. The training loss combines fused NLL, gate BCE, a consistency alignment, and an entropy penalty:

$$\mathcal{L}_{\text{mix}} = \mathbb{E}_i[w_i \cdot (-\log \mathbf{p}_{\text{mix},i}(y_i))],\quad (20)$$

$$\mathcal{L}_{\text{gate}} = \mathbb{E}_i[w_i \cdot \text{BCE}(g_i, \tilde{g}_i; \text{pos}_w)],\quad (21)$$

$$\mathcal{L}_{\text{align}} = \mathbb{E}_i[w_i \cdot \text{KL}(\mathbf{p}_i^* \parallel \mathbf{p}_{\text{mix},i})],\quad (22)$$

$$\mathcal{L}_{\text{ent}} = \mathbb{E}_i[\lambda_{\text{ent}} \cdot |\Delta_i^{(y)}| \cdot \text{H}_{\text{Bern}}(g_i)],\quad (23)$$

where $\mathbf{p}_i^* = \mathbf{p}_{\text{global},i}$ if $\tilde{g}_i > 0.5$ and $\mathbf{p}_i^* = \mathbf{p}_{\text{local},i}$ otherwise, and pos_w is an adaptive positive weight from the batch. The full objective is

$$\mathcal{L}_{\text{gate-fuse}} = \mathcal{L}_{\text{mix}} + \mathcal{L}_{\text{gate}} + \lambda_{\text{align}} \mathcal{L}_{\text{align}} + \mathcal{L}_{\text{ent}} + \lambda_{\text{aux}} \mathcal{L}_{\text{aux}},\quad (24)$$

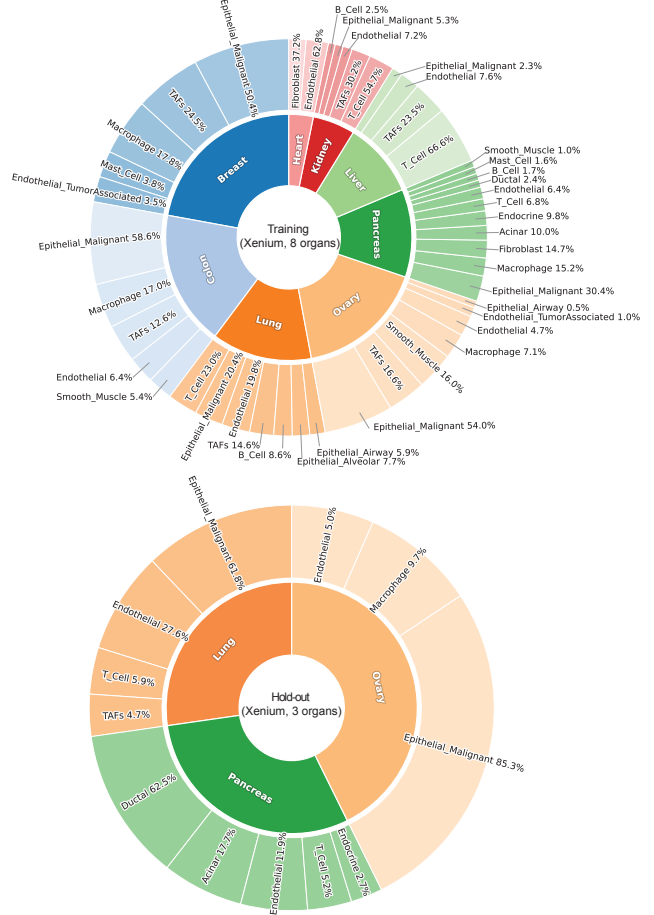


Figure 2. **Organ and cohort wise composition.** Donut plots of the training set (8 organs) and the hold-out testing cohorts (pancreas, ovary, lung). The figure illustrates the distribution shifts between training and evaluation cohorts.

with a small auxiliary term \mathcal{L}_{aux} added only when unfreezing heads/backbones.

Schedule and deployment (safe gate; GT-free). We first train the gate with Path local/Path global frozen (gate-only warm-up), then optionally unfreeze lightweight modules with small LRs. At test time we use Eq. (15). For deployment we provide a *safe gate* calibrated on validation data: compute per-path reliability by *predicted* class, form a baseline chooser by p_{\max}^{\times} reliability, and accept the gate’s choice only when

$$g_i > \tau \quad \text{and} \quad |\rho_i| > \gamma,$$

with $\rho_i = p_{\max}^{\text{global}} - p_{\max}^{\text{local}}$. This conservative policy is GT-free and empirically avoids regressions vs. the best single path while often improving accuracy.

Metric	FiLM	Concat	$\Delta(\text{F-C})$
ACC	0.8493	0.4845	+0.3648
F1-macro	0.5929	0.4076	+0.1853
Silhouette \uparrow	0.1480	0.0182	+0.1298
CH \uparrow	236.8	200.6	+36.2
DB \downarrow	4.26	5.56	-1.30
ECE \downarrow	0.061	0.213	-0.152

Table 1. FiLM improves feature separability and probability calibration without changing the training pipeline. Silhouette/CH/DB follow the classic definitions [6, 10, 34]; ECE follows [18].

4. Experiments

4.1. Experimental Setup

Datasets and splits. All methods are trained on the same multi-organ dataset covering breast, colon, heart, kidney, liver, lung, ovary, and pancreas, and evaluated on three disjoint *hold-out* Xenium cohorts (lung, ovary, and pancreas). Each image originates from a distinct patient, so there is no patient-level overlap between training and testing cohorts, and no images or annotations from any hold-out cohort are seen during training. To substantiate the gene-marker-based labeling scheme, Appendix lists all cell types together with their top 10 marker genes, providing an additional justification for our annotation strategy. Figure 2 summarizes the organ and cohort composition.

Cohort-specific label alignment. We standardize training labels to a canonical taxonomy and remove ambiguous categories. Each cohort uses a fixed set of fixed evaluation labels with a deterministic train \rightarrow evaluation mapping. Let $p_{\text{train}} = \text{softmax}(\text{logits}_{\text{train}})$ and let $\mathbf{M} \in \mathbb{R}^{K_{\text{train}} \times K_{\text{eval}}}$ be a sparse mapping matrix; evaluation-space probabilities are

$$p_{\text{eval}} = \mathbf{M}^T p_{\text{train}}, \quad (25)$$

where each column of \mathbf{M} sums probabilities of training classes that map to the same evaluation class. For each cohort, the evaluation label set is restricted to the intersection between the canonical taxonomy and the cell types present in that cohort, so that all methods are evaluated on the same set of labels.

Information parity & implementation. To equalize metadata usage, all *fine-tuned* models (ours and baselines) attach a learned **32-d organ embedding** to the visual feature and train it jointly with the classifier,¹ while DINO baselines use *frozen backbones with a linear probe* and therefore do not use organ embeddings, preserving the standard LP protocol. Fine-tuned runs share the same optimizer (AdamW), cosine learning-rate decay with warmup, early stopping on validation macro-F1, PyTorch 2.x with

¹Unless noted otherwise, we concatenate the organ embedding to the visual feature.

BF16 (TF32 on Ampere+), and identical dataloaders, precision settings, batch sizes, and training schedules per resolution [15, 24, 25, 32].

4.2. Comparison with SOTA Models

Baselines and training setup. All baselines are instantiated in the unified label space and data pipeline described above. For **MUSK**, **LOKI**, and **PLIP** we start from the official checkpoints and recommended training recipes from their original papers and public code, adjusting only image resolution, batch size, and training epochs to match the available GPU memory and keep the total number of optimization steps within the same order of magnitude as our method. The resulting configurations and GPU usage are summarized in Appendix.

Our model. We evaluate all three stages of our framework on the same hold-out cohorts: (1) a **Path local** expert specialized for small-scale, densely structured morphology at 224^2 resolution; (2) a **Path global** expert capturing large-field contextual patterns at 1024^2 ; and (3) a learned **Fusion Gate** that adaptively integrates the two paths by weighting logits per input. Hyperparameters and training details for these three components are provided in Appendix.

Fair comparison protocol. All models are trained on the *same* multi-organ corpus, follow the *same* taxonomy and fixed train \rightarrow eval mapping for each cohort, and use the *same* cohort alignment and evaluation pipeline. To ensure *information parity*, every fine-tuned model—**MUSK**, **PLIP**, **LOKI**, and ours—receives organ/tissue identity as prior knowledge. For **DINO** baselines, we keep the frozen-backbone linear-probe setting (no organ conditioning) to preserve the standard LP protocol. Quantitative results on all cohorts are summarized in Table 2.

Results summary and takeaways. Table 2 reports per-class F1 across all hold-out cohorts. Overall, our **Path local** and **Path global** experts remain strong and complementary, and the learned **Fusion Gate** typically matches or exceeds the better single path. For example, on **lung**, Fusion Gate improves malignant epithelium to **96.42** F1 and raises T cells from 43.89 (global) to **54.06** (+10.17). On **ovary**, it increases endothelial from 75.20/73.44 (local/global) to **77.96**. These gains reflect the benefit of combining fine-grained morphology with wide-field tissue context.

At the same time, *fusion is not uniformly superior to the best single path*. In **pancreas**, several morphology-dominant classes are better handled by **Path local**: endocrine (87.39 local vs. 68.90 fusion), fibroblast (71.58 vs. 68.65), and ductal (39.24 vs. 35.24); in **lung** CAFs, local (47.55) also exceeds fusion (44.86). We therefore (i) report per-cohort macro/micro F1 and confidence intervals in the Appendix, and (ii) deploy a calibrated *safe gate* that defers to the reliability-weighted single path unless the gate is con-

Table 2. Per-class F1 on hold-out datasets. *Legend:* DINO-B/L/S+/16 = DINOv3 ViT-B/L/S(16+); Path local and Path global are our single-path experts; Fusion Gate is our learned gating fusion. Best/second/third are marked as ■/■/■.

Organ	Cell type	SOTA models						Ours		
		Frozen backbone + LP			Fully fine-tuned			Path local	Path global	Fusion Gate
		DINO-B/16	DINO-L/16	DINO-S+/16	LOKI	PLIP	MUSK			
Lung	Epithelial Malignant	84.62	83.40	48.87	86.34	65.62	81.35	93.90	95.23	96.42^{+1.18}
	Endothelial	50.18	55.66	36.13	56.04	51.08	73.17	82.49	83.53	83.76^{+0.24}
	T Cell	9.72	9.28	11.99	25.49	21.73	28.18	13.23	43.89	54.06^{+10.17}
	CAFs	35.48	24.29	9.55	25.67	19.41	28.91	47.55^{+2.69}	43.74	44.86
Ovary	Epithelial Malignant	90.33	90.64	82.87	64.28	87.36	83.57	94.14	93.86	94.17^{+0.03}
	Macrophage	9.20	10.33	17.44	17.69	16.70	30.17	20.78	34.78	35.15^{+0.37}
	Endothelial	22.00	20.71	7.40	28.87	35.57	53.25	75.20	73.44	77.96^{+2.76}
Pancreas	Endothelial	9.68	6.63	8.33	15.28	19.67	22.49	49.38^{+0.66}	48.44	48.72
	T Cell	9.53	9.59	5.41	7.26	9.01	7.51	20.11	21.36	22.54^{+1.18}
	Fibroblast	46.53	45.37	60.86	57.48	13.20	65.14	71.58^{+2.94}	62.87	68.65
	Endocrine	0.00	0.00	8.92	0.00	1.24	20.26	87.39^{+6.54}	80.85	68.90
	Ductal	4.29	0.00	0.00	0.00	1.66	4.12	39.24^{+4.00}	31.33	35.24
	Acinar	0.00	0.00	16.46	0.00	1.01	18.97	44.30	42.65	44.60^{+0.30}

fidant and the two paths strongly disagree. Empirically this policy is no worse than the best single expert while often preserving the fusion gains on context-sensitive classes.

Takeaways. (1) Classes requiring architectural or microenvironmental cues (e.g., lymphocytes, ductal/endocrine, endothelial variants) benefit the most from global context and gated fusion. (2) For classes where nuclear morphology is decisive, the gate learns to favor Path local; safe gating further guards against over-fusion. (3) Under strong class imbalance and distribution shift (e.g., pancreas), multi-scale specialization with adaptive fusion remains robust on average, while acknowledging class-wise variability.

4.3. Ablation Studies

Tissue-aware FiLM in Path local. Replacing simple concatenation with a FiLM modulation between backbone and head improves separability and calibration [33]. Given feature $\mathbf{f} \in \mathbb{R}^{1536}$ and tissue embedding $\mathbf{e}_t \in \mathbb{R}^{64}$, FiLM predicts $(\gamma, \beta) = g_\theta(\mathbf{e}_t)$ and applies $\tilde{\mathbf{f}} = (1 + \gamma) \odot \mathbf{f} + \beta$. On a held-out lung subset, FiLM yields higher accuracy and macro-F1 and lower ECE (Table 1), with tighter clusters and a near-diagonal reliability curve (Fig. 3).

Complementarity of scales (local/global). Evaluating the best checkpoints of **Path local** and **Path global** on eight validation sets (16 classes total) shows clear disagreement structure: **Path global** dominates in 11/16 classes that require broader context (e.g., *cardiomyocyte*, *ductal*, *endocrine*, *T cell*), while **Path local** leads in 4/16 morphology-dense classes (e.g., *B cell*, *endothelial*, *smooth muscle*, *malignant epithelium*); *acinar* is roughly balanced. An oracle that picks the correct expert per sample yields a positive upper bound, explaining the strong gains of **Fusion Gate** (Fig. 4).

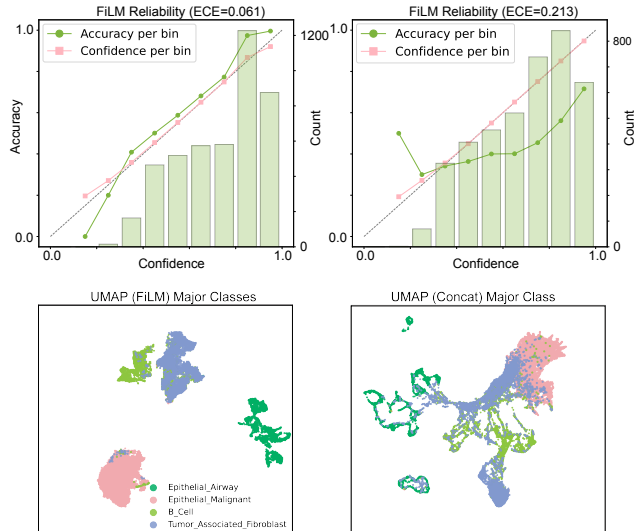


Figure 3. **Lung subset: reliability and feature geometry.** FiLM (left) vs. Concat (right). FiLM reduces ECE [18] (0.061 vs. 0.213) and produces more compact, tissue-aligned clusters.

Fusion-gate loss design. The fusion gate is trained with the composite loss $L = L_{\text{mix}} + L_{\text{gate}} + L_{\text{align}} + L_{\text{ent}}$, where L_{mix} applies cross-entropy to the fused prediction, L_{gate} supervises a soft target that favors the more reliable expert, L_{align} encourages the fused distribution to stay close to the selected expert, and L_{ent} regularizes the gate’s entropy. We evaluate the contribution of each component through a drop-one ablation on the eight-organ validation set, using precomputed features and training only the gate and classification heads. Table 3 reports the detailed results.

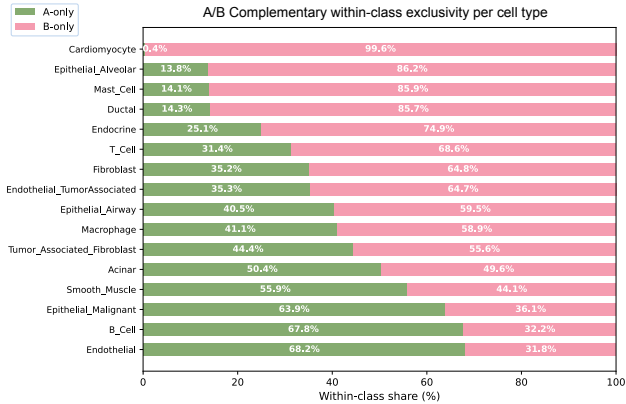


Figure 4. Within-class shares of *local-only* (Path local correct, Path global wrong) vs *global-only* (Path global correct, Path local wrong). The asymmetry indicates complementary failure modes, motivating gated fusion.

L_{mix}	L_{gate}	L_{align}	L_{ent}	Gate		Safe		ECE (Gate / Safe)	
				Acc	F1	Acc	F1	Gate	Safe
✓	✓	✓	✓	0.8641	0.7843	0.8645	0.7617	0.0304	0.0603
×	✓	✓	✓	0.0001	0.0000	0.0001	0.0000	0.6400	0.6515
✓	×	✓	✓	0.8663	0.7880	0.8647	0.7794	0.0221	0.0333
✓	✓	×	✓	0.8662	0.7867	0.8552	0.7079	0.0298	0.0951
✓	✓	✓	×	0.8635	0.7831	0.8640	0.7572	0.0285	0.0606

Table 3. **Fusion-gate loss ablation.** Columns report performance of the gated prediction (*Gate*) and the Safe fusion [31] output, together with calibration error (ECE↓). Removing L_{mix} collapses the model, confirming the need for supervision on the fused prediction. The other terms shape how the gate balances the two experts: L_{align} has a strong impact on Safe-fusion calibration, while L_{gate} and L_{ent} act as mild regularizer that stabilize gating without harming accuracy or F1.

4.4. Visualization

To examine *where* different models focus, we visualize token-level Grad-CAM overlays from the last transformer block on representative 224^2 ovary patches (Fig. 5) [35]. Across all examples, **Path local** produces compact, high-intensity responses that align with histologically meaningful structures, such as clusters of nuclei, epithelial–stromal interfaces, and sharp tissue borders. In contrast, LOKI, MUSK, and PLIP often yield more diffuse or fragmented activations that primarily follow coarse color/textural patterns and frequently extend into stromal or background regions with limited diagnostic value. This tighter spatial correspondence between **Path local** attention and nuclear morphology/boundaries is consistent with its stronger per-class F1 performance. More examples can be found at Appendix.

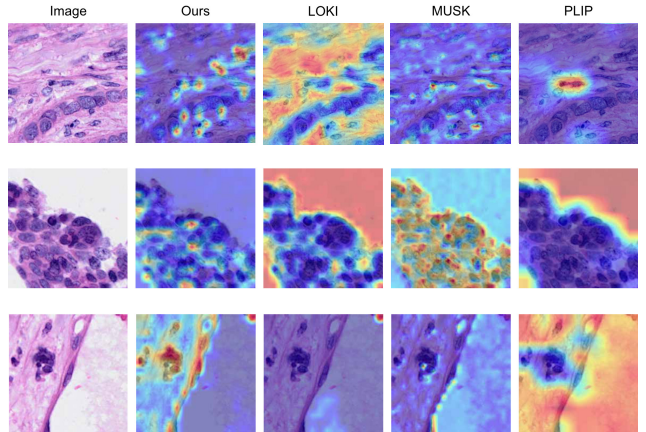


Figure 5. **Token-level Grad-CAM on ovary patches.** Columns: input, **Path local**, LOKI, MUSK, PLIP. Overlays (last block, $\alpha=0.45$) on 224^2 patches. Compared with the baselines, **Path local** concentrates its responses on clusters of nuclei and tissue interfaces, whereas LOKI, MUSK, and PLIP often highlight broad texture patterns or even background regions, indicating weaker alignment with diagnostic structures.

5. Conclusion and Discussion

We presented **NuClass**, a cell-wise multi-scale framework that treats nuclear morphology and tissue context as independent experts and fuses them through a GT-free, probability-space gate. This design cleanly separates expert specialization from fusion, offers stable training via freeze–then–optional–unfreeze scheduling, and enables a conservative, reliability-calibrated deployment rule. Across three fully held-out cohorts, NuClass consistently matches or exceeds strong frozen and fine-tuned baselines, achieving up to 96% F1 for its best-performing class and maintaining robust generalization under distribution shift. Our experiments reveal three central findings:

- **Scale complementarity.** Local morphology and global context excel on different phenotypes; the oracle gains (Fig. 4) indicate substantial untapped complementarity.
- **Adaptive but selective fusion.** Fusion improves context-sensitive classes, whereas morphology-dominant classes remain better served by the local path, underscoring the need for per-class evaluation.
- **Safe deployment.** A reliability-aware gating policy preserves nearly all fusion benefits while preventing regressions below the strongest single expert.

NuClass is directly usable as a plug-in module for existing cell-level pipelines and provides a principled mechanism for deferral when confidence is low. Nonetheless, limitations remain: marker-guided labels inherit Xenium biases; context modeling increases computational cost; and the dataset, while multi-organ, still lacks broader staining, scanner, and population diversity.

Future work will expand NuClass toward pan-cancer coverage, refine taxonomies to finer subtypes and cellular states, extend to end-to-end H&E-only pipelines with automatic nucleus detection, and explore adaptive context fields, efficient distillation, and stronger uncertainty calibration for clinical deployment. We also aim to incorporate active learning and uncertainty-guided sampling to more efficiently expand the training corpus with high-value annotations and reduce reliance on large-scale marker-based labeling.

References

- [1] 10x Genomics. Xenium in situ: High-plex spatial gene expression platform (technical overview). Technical report, 10x Genomics, 2022. Technical white paper; subcellular transcript detection and panel design. [2](#)
- [2] Mohamed Amgad, Lamees A Atteya, Hagar Hussein, Kareem Hosny Mohammed, Ehab Hafiz, Maha A T Elsebaie, Ahmed M Alhusseiny, Mohamed Atef AlMoslemany, Abdelmagid M Elmatboly, Philip A Pappalardo, Rokia Adel Sakr, Pooya Mobadersany, Ahmad Rachid, Anas M Saad, Ahmad M Alkashash, Inas A Ruhban, Anas Alrefai, Nada M Elgazar, Ali Abdulkarim, Abo-Alela Farag, Amira Etman, Ahmed G Elsaheed, Yahya Alagha, Yomna A Amer, Ahmed M Raslan, Menatalla K Nadim, Mai A T Elsebaie, Ahmed Ayad, Liza E Hanna, Ahmed Gadallah, Mohamed Elkady, Bradley Drumheller, David Jaye, David Manthey, David A Gutman, Habiba Elfandy, and Lee A D Cooper. Nucls: A scalable crowdsourcing approach and dataset for nucleus classification and segmentation in breast cancer. *GigaScience*, 11, 2022. [3](#)
- [3] Jimmy Lei Ba, Jamie Ryan Kiros, and Geoffrey E. Hinton. Layer normalization. *arXiv:1607.06450*, 2016. [3](#)
- [4] Hang Bao, Li Dong, and Furu Wei. BEiT: BERT pre-training of image transformers. In *ICLR*, 2022. [3](#)
- [5] Yoshua Bengio, Jérôme Louradour, Ronan Collobert, and Jason Weston. Curriculum learning. In *ICML*, 2009. [4](#)
- [6] Tadeusz Caliński and Jerzy Harabasz. A dendrite method for cluster analysis. *Communications in Statistics*, 3(1):1–27, 1974. [6](#)
- [7] Richard J. Chen, Chengkuan Chen, Yicong Li, Tiffany Y. Chen, Andrew D. Trister, Rahul G. Krishnan, and Faisal Mahmood. Scaling vision transformers to gigapixel images via hierarchical self-supervised learning. In *Proceedings of the IEEE/CVF Conference on Computer Vision and Pattern Recognition (CVPR)*, pages 16144–16155, 2022. [1](#)
- [8] Richard J Chen, Tong Ding, Ming Y Lu, Drew FK Williamson, Guillaume Jaume, Bowen Chen, Andrew Zhang, Daniel Shao, Andrew H Song, Muhammad Shaban, et al. Towards a general-purpose foundation model for computational pathology. *Nature Medicine*, 2024. [3](#)
- [9] Yin Cui, Menglin Jia, Tsung-Yi Lin, Yang Song, and Serge Belongie. Class-balanced loss based on effective number of samples, 2019. [3](#), [4](#)
- [10] David L. Davies and Donald W. Bouldin. A cluster separation measure. *IEEE Transactions on Pattern Analysis and Machine Intelligence*, PAMI-1(2):224–227, 1979. [6](#)
- [11] Tong Ding, Sophia J Wagner, Andrew H Song, Richard J Chen, Ming Y Lu, Andrew Zhang, Anurag J Vaidya, Guillaume Jaume, Muhammad Shaban, Ahrong Kim, et al. A multimodal whole-slide foundation model for pathology. *Nature Medicine*, pages 1–13, 2025. [3](#)
- [12] Alexey Dosovitskiy, Lucas Beyer, Alexander Kolesnikov, Dirk Weissenborn, Xiaohua Zhai, Thomas Unterthiner, Mostafa Dehghani, Matthias Minderer, Georg Heigold, Sylvain Gelly, Jakob Uszkoreit, and Neil Houlsby. An image is worth 16x16 words: Transformers for image recognition at scale. In *ICLR*, 2021. [3](#)
- [13] Jevgenij Gamper, Navid Alemi Koohbanani, Ksenija Benet, Ali Khuram, and Nasir Rajpoot. Pannuke: An open pan-cancer histology dataset for nuclei instance segmentation and classification. In *Digital Pathology*, pages 11–19. Springer International Publishing, Cham, 2019. [2](#), [3](#)
- [14] Jevgenij Gamper, Navid Alemi Koohbanani, Ksenija Benes, Simon Graham, Mostafa Jahanifar, Syed Ali Khuram, Ayesha Azam, Katherine Hewitt, and Nasir Rajpoot. Pannuke dataset extension, insights and baselines, 2020. [3](#)
- [15] Priya Goyal, Piotr Dollár, Ross Girshick, Pieter Noordhuis, Lukasz Wesolowski, Aapo Kyrola, Andrew Tulloch, Yangqing Jia, and Kaiming He. Accurate, large minibatch SGD: Training ImageNet in 1 hour. In *arXiv:1706.02677*, 2017. [6](#)
- [16] Simon Graham, Quoc Dang Vu, Shan E. A. Raza, and et al. Hover-net: Simultaneous segmentation and classification of nuclei in multi-tissue histology images. *Medical Image Analysis*, 58:101563, 2019. [2](#), [3](#)
- [17] Simon Graham, Mostafa Jahanifar, Ayesha Azam, Mohammed Nimir, Yee-Wah Tsang, Katherine Dodd, Emily Hero, Harvir Sahota, Atisha Tank, Ksenija Benes, Noorul Wahab, Fayyaz Minhas, Shan E Ahmed Raza, Hesham El Daly, Kishore Gopalakrishnan, David Snead, and Nasir Rajpoot. Lizard: A large-scale dataset for colonic nuclear instance segmentation and classification, 2021. [3](#)
- [18] Chuan Guo, Geoff Pleiss, Yu Sun, and Kilian Q. Weinberger. On calibration of modern neural networks, 2017. [6](#), [7](#)
- [19] Fabian Hörst, Moritz Rempe, Lukas Heine, and et al. Cellvit: Vision transformers for precise cell segmentation and classification. *Medical Image Analysis*, 94:103143, 2024. [3](#)
- [20] Gao Huang, Yu Sun, Zhuang Liu, Daniel Sedra, and Kilian Q. Weinberger. Deep networks with stochastic depth. In *ECCV*, 2016. [4](#)
- [21] Fabian Hörst, Moritz Rempe, Lukas Heine, Constantin Seibold, Julius Keyl, Giulia Baldini, Selma Ugurel, Jens Siveke, Barbara Grünwald, Jan Egger, and Jens Kleesiek. Cellvit: Vision transformers for precise cell segmentation and classification. *Medical Image Analysis*, 94:103143, 2024. [2](#)
- [22] Alexander Kolesnikov, Lucas Beyer, Xiaohua Zhai, Joan Puigcerver, Jessica Yung, Sylvain Gelly, and Neil Houlsby. Big transfer (BiT): General visual representation learning. In *NeurIPS (arXiv:1912.11370)*, 2020. [3](#)
- [23] Tsung-Yi Lin, Priya Goyal, Ross Girshick, Kaiming He, and Piotr Dollár. Focal loss for dense object detection. In *ICCV*, 2017. [4](#)

- [24] Ilya Loshchilov and Frank Hutter. Sgdr: Stochastic gradient descent with warm restarts. In *ICLR*, 2017. 6
- [25] Ilya Loshchilov and Frank Hutter. Decoupled weight decay regularization. *ICLR*, 2019. 6
- [26] Wei Lou, Xiang Wan, Guanbin Li, Xiaoying Lou, Chenghang Li, Feng Gao, and Haofeng Li. Structure embedded nucleus classification for histopathology images, 2023. 3
- [27] Ming Y. Lu, Bowen Chen, Andrew Zhang, Drew F. K. Williamson, Richard J. Chen, Tong Ding, Long Phi Le, Yung-Sung Chuang, and Faisal Mahmood. Visual language pretrained multiple instance zero-shot transfer for histopathology images, 2023. 3
- [28] Ming Y. Lu et al. A multimodal generative ai copilot for human pathology. *Nature*, 2024. 3
- [29] Rafael Müller, Simon Kornblith, and Geoffrey Hinton. When does label smoothing help? *NeurIPS*, 2019. 3, 4
- [30] Ramin Nakhli, Allen Zhang, Hossein Farahani, Amirali Darbandsari, Elahe Shenasa, Sidney Thiessen, Katy Milne, Jessica McAlpine, Brad Nelson, C Blake Gilks, and Ali Bashashati. Volta: an environment-aware contrastive cell representation learning for histopathology, 2023. 3
- [31] Jonas Nygård, Viktor Deleskog, and Gustaf Hendeby. Safe fusion compared to established distributed fusion methods. In *Proceedings of the IEEE International Conference on Multisensor Fusion and Integration for Intelligent Systems (MFI)*, 2016. 8
- [32] Adam Paszke, Sam Gross, Francisco Massa, Adam Lerer, James Bradbury, Gregory Chanan, Trevor Killeen, Zeming Lin, Natalia Gimelshein, Luca Antiga, et al. Pytorch: An imperative style, high-performance deep learning library. In *NeurIPS*, pages 8024–8035, 2019. 6
- [33] Ethan Perez, Florian Strub, Harm de Vries, Vincent Dumoulin, and Aaron Courville. Film: Visual reasoning with a general conditioning layer, 2017. 3, 7
- [34] Peter J. Rousseeuw. Silhouettes: A graphical aid to the interpretation and validation of cluster analysis. *Journal of Computational and Applied Mathematics*, 20:53–65, 1987. 6
- [35] Ramprasaath R. Selvaraju, Michael Cogswell, Abhishek Das, Ramakrishna Vedantam, Devi Parikh, and Dhruv Batra. Grad-cam: Visual explanations from deep networks via gradient-based localization. *International Journal of Computer Vision*, 128(2):336–359, 2019. 8
- [36] Claude E. Shannon. A mathematical theory of communication. *Bell System Technical Journal*, 27:379–423, 623–656, 1948. 3
- [37] Oriane Siméoni, Huy V. Vo, Maximilian Seitzer, Federico Baldassarre, Maxime Oquab, Cijo Jose, Vasil Khalidov, Marc Szafraniec, Seungeun Yi, Michaël Ramamonjisoa, et al. DINOv3. *arXiv:2508.10104*, 2025. 4
- [38] Nitish Srivastava, Geoffrey Hinton, Alex Krizhevsky, Ilya Sutskever, and Ruslan Salakhutdinov. Dropout: A simple way to prevent neural networks from overfitting. *JMLR*, 15: 1929–1958, 2014. 4
- [39] Hugo Touvron, Matthieu Cord, and Hervé Jégou. DeiT III: Revenge of the ViT. *arXiv:2212.04884*, 2022. 3
- [40] Ashish Vaswani, Noam Shazeer, Niki Parmar, Jakob Uszkoreit, Llion Jones, Aidan N. Gomez, Łukasz Kaiser, and Illia Polosukhin. Attention is all you need. In *NeurIPS*, 2017. 4
- [41] Ruchika Verma, Neeraj Kumar, Abhijeet Patil, et al. Monusac2020: A multi-organ nuclei segmentation and classification challenge. *IEEE Transactions on Medical Imaging*, 40(12):3413–3423, 2021. 2
- [42] Eugene Vorontsov, Alican Bozkurt, Adam Casson, et al. A foundation model for clinical-grade computational pathology and rare cancers detection. *Nature Medicine*, 30(10): 2924–2935, 2024. 3
- [43] Martin Weigert and Uwe Schmidt. Nuclei instance segmentation and classification in histopathology images with stardist. In *2022 IEEE International Symposium on Biomedical Imaging Challenges (ISBIC)*, page 1–4. IEEE, 2022. 1
- [44] J. Xiang, X. Wang, X. Zhang, et al. A vision–language foundation model for precision oncology. *Nature*, 638:769–778, 2025. 3
- [45] Huanran Xu et al. A whole-slide foundation model for digital pathology from real-world data. *Nature*, 2024. 3

Adaptive Multi-Scale Integration Unlocks Robust Cell Annotation in Histopathology Images

Supplementary Material

Overview of the Supplementary Material

- **Baselines: provenance and rationale** (Sec. A; Tab. A1):
we describe how DINOv3 variants (frozen linear probe), PLIP, LOKI, and MUSK are instantiated under a unified protocol, including backbone choices, training protocol (frozen features vs. fine-tuning), and the rationale for each baseline family.
- **Full training and inference hyperparameters** (Sec. B; Tabs. A2–A4):
we provide complete optimization settings for the path-local expert, path-global expert, and Fusion Gate, covering optimizers, learning rates, layer-wise decay, warm-up schedules, batch size / precision, data augmentation, tissue conditioning (FiLM), loss formulations, and early stopping. We also describe the organ/tissue prior and the “unknown organ” ablation switch used at inference time.
- **Safe Gate calibration and deployment** (Sec. B, following Tabs. A2–A4):
we detail the counting of experts and the Safe Gate training configuration, and explain the validation-only procedure used to select conservative operating points for the gating policy at test time.
- **Compute budget and complexity** (Tab. A5):
we report parameter counts (trainable vs. non-trainable), total parameter size, peak GPU memory usage, wall-clock training time, and data scale for the *local*, *global*, and *gate* variants, together with the explicit counting policy that explains why Gate has $\sim 1.67\text{B}$ non-trainable parameters.
- **Dataset composition, cohort splits, and marker genes** (Sec. C; Tabs. A6–A8):
we summarize per-cohort cell counts, the number of unique cell types, and the train vs. hold-out composition after label rebuilding, and we list representative class-level marker genes used for molecular cell-type annotation.
- **Train→eval projection (unified with main Eq. (25))** (Sec. D; Eq. A1):
we formalize the canonical projection $p_{\text{eval}} = M^{\top} p_{\text{train}}$, provide a minimal numeric example (including tensor shapes), and give explicit cohort-wise binary projection matrices M_{lung} , M_{ovary} , and M_{pancreas} that map the canonical training taxonomy to each evaluation taxonomy.
- **Cohort-wise Macro/Micro-F1, accuracy, and local-aware gating** (Sec. E; Sec. E.1; Tab. A11):
we report macro-F1 and micro-F1 (accuracy) with 95% confidence intervals from non-parametric bootstrap ($B=1000$) for each held-out cohort and overall, and analyze how the local-aware gating signal affects the global path in terms of accuracy, macro-F1, calibration (ECE, Brier score), AUROC, and performance on low-confidence / high-entropy subsets.
- **Additional visualizations** (Sec. E.1; Figs. A1–A2):
we provide additional Grad-CAM visualizations for the path-local expert and for LOKI, MUSK, and PLIP on representative examples, illustrating qualitative differences in attention patterns across methods.

A. Baselines: provenance and rationale

Model	Type	Backbone	Training protocol	Rationale
DINOv3-B/16	SSL ViT (frozen)	ViT-B/16	Frozen features + linear probe	Canonical LP baseline
DINOv3-L/16	SSL ViT (frozen)	ViT-L/16	Frozen features + linear probe	Larger-scale LP variant
DINOv3-S+/16	SSL ViT (frozen)	ViT-S+/16	Frozen features + linear probe	Smaller LP variant
PLIP	VLP (fine-tuned)	ViT-L/14	Vision tower fine-tuning	Pathology VLP transfer
LOKI	VLP (fine-tuned)	ViT-L/14-like	Vision tower fine-tuning	Visual-omics VLP baseline
MUSK	Vision-only (FT)	p16 transformer	End-to-end fine-tuning	Strong non-VLP foundation model

Table A1. Snapshot of baseline families and protocols used in our experiments. All fine-tuned baselines employ the same 32-d organ embedding, data pipeline, and optimization setup for parity; DINOv3 variants are evaluated with frozen backbones and a learned linear probe.

B. Full training and inference hyperparameters

Backbone	UNI2-h (ViT-L/14-like, 224^2 , embed=1536)
Optimizer / Weight Decay	AdamW / 2×10^{-5}
LR (UNI / Head)	3×10^{-6} / 3×10^{-4}
Layer-wise LR decay γ	0.85 (earlier layers \rightarrow lower LR)
Scheduler	Linear warm-up to 1.0 (steps=1500); no decay
Epochs / Freeze	50 / freeze backbone for the first epoch
Batch (effective) / Precision	$512 \times 2 = 1024$ / BF16-mixed
Data augmentation	H/V flip, $\pm 15^\circ$ rotation, color jitter, affine, normalization
Tissue conditioning	FiLM (embedding dim 64)
Loss	Class-balanced CE (Effective Number, $\beta=0.9999$) + label smoothing $\varepsilon=0.1$
Early stopping / Validation cadence	patience 4 / every 0.25 epoch

Table A2. Path-local hyperparameters.

Backbones	UNI2-h (224^2) + DINOv3-L/16 (context)
Optimizer / Weight Decay	AdamW / 2×10^{-5}
LR (UNI / Head / DINO)	2×10^{-6} / 3×10^{-4} / 1×10^{-6} (DINO frozen by default)
Layer-wise LR decay γ	0.85 (UNI)
Scheduler	Linear warm-up (steps=2000); no decay
Epochs / Precision	40 / BF16-mixed
Batch (effective)	$256 \times 2 = 512$
Context size / micro-batch	1024 / 16 (DINO forward chunking)
Fusion α warm-up	$\alpha: 0.25 \rightarrow 1.0$ (first 2 epochs)
Context dropout	0.10
Freeze policy	UNI unfrozen; DINO frozen (optional unfreeze)
Loss	$w = (1 - p_A(y))^\gamma$, $\gamma=2.0$; $\mathcal{L} = \mathcal{L}_{\text{main}} + 0.3 \mathcal{L}_B$

Table A3. Path-global hyperparameters.

Organ/tissue prior and ablation note. In routine surgical pathology, organ/tissue identity is recorded at accession and remains available during H&E processing; we therefore treat it as known metadata and encode it via a 32-d embedding for

Inputs / Backbones	A: UNI2-h+FiLM; B: UNI2-h + DINOv3-L context
Optimizer / Weight Decay	AdamW / 1×10^{-5}
LRs (gate / heads / backbone)	8×10^{-4} / 2×10^{-4} / 5×10^{-5}
Scheduler	Linear warm-up (steps=1000)
Epochs / Batch (effective)	4 / $12 \times 32 = 384$
Context size / micro-batch	384 / 16 (context resized on CPU)
Gate warm-up	first 0.5 epoch gate-only, then optional unfreeze
Gate MLP	projA(1536→128)+projB(1024→128)→MLP(256,64,1); dropout 0.1 (gate), 0.2 (head)
Losses	$\mathcal{L}_{\text{mix}} + \mathcal{L}_{\text{gate}} + \lambda_{\text{align}} \mathcal{L}_{\text{align}} + \mathcal{L}_{\text{ent}} + \lambda_{\text{aux}} \mathcal{L}_{\text{aux}}$
Weights	$\lambda_{\text{align}} = 0.1$, $\lambda_{\text{ent}} = 0.05$, $\lambda_{\text{aux}} = 0.05$; conflict boost = 2.0

Table A4. Fusion Gate hyperparameters.

Table A5. Compute and memory budget of the **local**, **global**, and **gate** variants. Parameter counts follow PyTorch Lightning summaries; memory numbers are peak usage on a single H200 (141 GB).

Setup	Trainable params	Non-trainable params	Total params	Param size
local (baseline)	683M	0	683M	2.73 GB
global (ours)	686M	303M	989M	3.96 GB
gate (ours)	$\approx 0.42\text{M}$	$\approx 1.67\text{B}$	$\approx 1.67\text{B}$	$\approx 6.7\text{GB}$

Setup	GPU(s)	Peak memory (of 141 GB)	Wall-clock time	Data scale
local (baseline)	1 × H200	15% ($\approx 21\text{ GB}$)	$\sim 5\text{ h}$	1.60M train / 0.45M val (16 classes)
global (ours)	1 × H200	40% ($\approx 56\text{ GB}$)	$\sim 22\text{ h}$	1.60M train / 0.45M val (16 classes)
gate (ours)	1 × H200	69% ($\approx 97\text{ GB}$)	$\sim 5\text{ h}$	1.60M train / 0.45M val (16 classes)

all fine-tuned models (“information parity”). To simulate “unknown organ” without retraining, our released inference code provides a switch that replaces the organ embedding with a learned [UNK] token (or a zero-vector through FiLM), allowing users to assess sensitivity to this prior.

Counting policy for Table A6 (why Gate shows 1.67B non-trainable). Table A6 reports parameter counts from PyTorch Lightning “summary” under the *modules resident in memory* during each stage. Gate training instantiates **both** experts end-to-end and freezes them: Path A uses UNI2-h, Path B uses UNI2-h *and* DINOv3-L/16 for context. Hence the non-trainable pool is

$$\underbrace{\text{UNI2-h}}_{\text{Path local}} + \underbrace{\text{UNI2-h}}_{\text{Path global}} + \underbrace{\text{DINOv3-L/16}}_{\text{Path global}} \approx 2 \times 683\text{M} + 303\text{M} = 1,669\text{M},$$

matching the Gate row (non-trainable/total/size). Only the small Gate MLP and heads ($\sim 0.42\text{M}$) are trainable.

C. Dataset composition and cohort splits

Cohort (organ)	Cells	Unique types
Ovarian_wsi (ovary)	384,805	7
Pancreas_wsi (pancreas)	187,522	11
Heart-MultiCancerPanel (heart)	5,859	2
Kidney-MultiCancerPanel-Cancer (kidney)	27,550	5
Liver-MultiCancerPanel-Cancer (liver)	96,716	4
Lung-Cancer-v1+5k (lung)	195,133	7
Colon_Preview (colon)	446,933	5
Breast_Entire-Sample-Area-S1 (breast)	701,220	5
Combined	2,045,738	16

Table A6. Training cohorts after mapping/filtering.

Cohort (organ)	Cells	Unique types
Pancreatic_Multimodal_Cell_Segmentation (pancreas)	74,689	6
Ovarian-ImmunoOnco+CustomAddon (ovary)	150,748	3
Lung-ImmunoOnco+CustomAddon (lung)	61,490	4
Combined	286,927	9

Table A7. Hold-out cohorts.

Class	Top 10 marker genes
Epithelial_Malignant	EPCAM, KRT8, KRT18, KRT19, KRT17, KRT5, MKI67, MCM2, TOP2A, BIRC5
Cancer_Associated_Fibroblast	COL1A1, COL1A2, COL3A1, ACTA2, TAGLN, PDGFRB, FAP, PDPN, POSTN, CXCL12
Macrophage	CD68, LST1, CSF1R, MS4A7, C1QA, C1QB, C1QC, CD163, MRC1, ITGAM
T_Cell	CD3D, CD3E, CD2, CD4, CD8A, TRAC, CD247, LCK, IL7R, CCR7
Endothelial	PECAM1, VWF, KDR, CD34, EMCN, FLT1, KLF2, CLDN5, ENG, ESAM
Smooth_Muscle	ACTA2, TAGLN, MYH11, CNN1, MYL9, DES, TPM2, CALD1, RGS5, MYLK
Mast_Cell	KIT, TPSAB1, TPSB2, CPA3, MS4A2, HDC, GATA2, FCER1A, SRGN, SLC18A2
Fibroblast	COL1A1, COL1A2, DCN, LUM, PDGFRA, COL3A1, COL5A1, FBLN1, THY1, VIM
Endothelial_CancerAssociated	PECAM1, VWF, KDR, ICAM1, SELE, FLT1, VCAM1, ANGPT2, IL6, CXCL8
B_Cell	MS4A1, CD79A, CD79B, CD74, CD19, CD22, CD37, CD40, BANK1, PAX5
Acinar	PRSS1, PRSS3, CPA1, CPB1, CELA3A, CTRB1, CTRC, CEL, CPA2, REG1A
Endocrine	INS, GCG, SST, PPY, CHGA, IAPP, PCSK1, PCSK2, PAX6, MAFA
Epithelial_Alveolar	SFTPA1, SFTPA2, SFTPB, SFTPC, SLC34A2, AGER, LPCAT1, ABCA3, KRT8, KRT18
Epithelial_Airway	KRT5, KRT8, KRT18, MUC1, SCGB1A1, KRT14, KRT15, KRT17, FOXJ1, EPCAM
Ductal	KRT7, KRT8, KRT18, KRT19, MUC1, EPCAM, KRT23, SOX9, CFTR, SPP1
epithelial	EPCAM, KRT8, KRT18, KRT19, KRT5, KRT14, KRT15, KRT17, CDH1, KRT7
lymphocyte	PTPRC, CD3D, CD3E, MS4A1, CD79A, CD4, CD8A, NKG7, GNLY, TRAC
plasma	MZB1, XBP1, SDC1, SLAMF7, PRDM1, IGKC, IGHG1, JCHAIN, TNFRSF17, CD38

Table A8. Class-level marker genes used for cell type annotation. We list the top 10 marker genes per class here for brevity; in our actual analysis we use the top 50 marker genes.

D. Cohort-specific projection matrices

Definition and notation (unified). Let C_{train} and C_{eval} be the numbers of classes in the training and evaluation taxonomies for a given cohort. We define a fixed binary projection

$$M \in \{0, 1\}^{C_{\text{train}} \times C_{\text{eval}}}, \quad M_{ij} = 1 \text{ iff training class } i \text{ maps to evaluation class } j.$$

Given $p_{\text{train}} \in \Delta^{C_{\text{train}}-1}$, the evaluation-space probabilities are

$$p_{\text{eval}} = M^\top p_{\text{train}} \in \mathbb{R}^{C_{\text{eval}}}, \quad (\text{A1})$$

so $(p_{\text{eval}})_j = \sum_{i: M_{ij}=1} (p_{\text{train}})_i$. We rebuild labels so that each retained training class maps to *exactly one* evaluation class; thus $\sum_j M_{ij} \in \{0, 1\}$ and $\sum_j (p_{\text{eval}})_j = 1$.

Minimal reproducible example (shapes and a numeric toy). Suppose $C_{\text{train}} = 5$ and $C_{\text{eval}} = 4$, where two epithelial subclasses are merged at evaluation:

$$M = \begin{bmatrix} 1 & 0 & 0 & 0 \\ 0 & 1 & 0 & 0 \\ 0 & 1 & 0 & 0 \\ 0 & 0 & 1 & 0 \\ 0 & 0 & 0 & 1 \end{bmatrix} \in \{0, 1\}^{5 \times 4}, \quad p_{\text{train}} = \begin{bmatrix} 0.10 \\ 0.15 \\ 0.35 \\ 0.25 \\ 0.15 \end{bmatrix} \Rightarrow p_{\text{eval}} = M^\top p_{\text{train}} = \begin{bmatrix} 0.10 \\ 0.50 \\ 0.25 \\ 0.15 \end{bmatrix}.$$

Cohort matrices. For each held-out cohort (lung, ovary, pancreas), we instantiate M with shape $C_{\text{train}} \times C_{\text{eval}}$ exactly as printed below; rows enumerate training classes in the canonical taxonomy and columns enumerate that cohort's evaluation classes (intersection set). The resulting $p_{\text{eval}} = M^\top p_{\text{train}}$ is used consistently in all tables and CI summaries.

Lung.

$$M_{\text{lung}} \in \{0, 1\}^{6 \times 4} = \left[\begin{array}{c|cccc} & \text{Endothelial} & \text{Epithelial_Malignant} & \text{T_Cell} & \text{Tumor_Associated_Fibroblast} \\ \hline \text{Epithelial_Malignant} & 0 & 1 & 0 & 0 \\ \text{Endothelial} & 1 & 0 & 0 & 0 \\ \text{Fibroblast} & 0 & 0 & 0 & 0 \\ \text{Macrophage} & 0 & 0 & 0 & 0 \\ \text{T_Cell} & 0 & 0 & 1 & 0 \\ \text{Tumor_Associated_Fibroblast} & 0 & 0 & 0 & 1 \end{array} \right].$$

Ovary.

$$M_{\text{ovary}} \in \{0, 1\}^{4 \times 3} = \left[\begin{array}{c|ccc} & \text{Endothelial} & \text{Epithelial_Malignant} & \text{Macrophage} \\ \hline \text{Epithelial_Malignant} & 0 & 1 & 0 \\ \text{Fibroblast} & 0 & 0 & 0 \\ \text{Macrophage} & 0 & 0 & 1 \\ \text{Endothelial} & 1 & 0 & 0 \end{array} \right].$$

Pancreas.

$$M_{\text{pancreas}} \in \{0, 1\}^{7 \times 6} = \left[\begin{array}{c|cccccc} & \text{Acinar} & \text{Ductal} & \text{Endocrine} & \text{Endothelial} & \text{Fibroblast_like} & \text{T_Cell} \\ \hline \text{Ductal} & 0 & 1 & 0 & 0 & 0 & 0 \\ \text{Fibroblast} & 0 & 0 & 0 & 0 & 1 & 0 \\ \text{Acinar} & 1 & 0 & 0 & 0 & 0 & 0 \\ \text{Tumor_Associated_Fibroblast} & 0 & 0 & 0 & 0 & 1 & 0 \\ \text{Endothelial} & 0 & 0 & 0 & 1 & 0 & 0 \\ \text{T_Cell} & 0 & 0 & 0 & 0 & 0 & 1 \\ \text{Endocrine} & 0 & 0 & 1 & 0 & 0 & 0 \end{array} \right].$$

E. Cohort-wise Macro/Micro-F1 and Accuracy with 95% Confidence Intervals

We report macro-F1 and micro-F1 for all cohorts using non-parametric bootstrap ($B=1000$ resamples per cohort). All entries are formatted as **mean (lower, upper)**, where values in parentheses denote the 95% confidence interval; best in each row is in **bold**. Evaluation strictly follows $p_{\text{eval}} = M^{\top} p_{\text{train}}$.

Table A9. Macro-F1 (mean (lower, upper), 95% CI).

Cohort	DINO-B/16	DINO-L/16	DINO-S+/16	LOKI	PLIP	MUSK	Path Local	Path Global	Fusion Gate
Lung	0.4500 (0.4465, 0.4535)	0.4316 (0.4281, 0.4351)	0.2663 (0.2628, 0.2698)	0.4839 (0.4804, 0.4874)	0.3945 (0.3910, 0.3980)	0.5290 (0.5255, 0.5325)	0.5930 (0.5883, 0.5981)	0.6658 (0.6610, 0.6684)	0.6971 (0.6913, 0.7026)
Ovary	0.4051 (0.4016, 0.4086)	0.4056 (0.4021, 0.4091)	0.3590 (0.3555, 0.3625)	0.3696 (0.3661, 0.3731)	0.4652 (0.4617, 0.4687)	0.5567 (0.5532, 0.5602)	0.6337 (0.6296, 0.6377)	0.6743 (0.6728, 0.6762)	0.6910 (0.6867, 0.6948)
Pancreas	0.1167 (0.1132, 0.1202)	0.1033 (0.0998, 0.1068)	0.1667 (0.1632, 0.1702)	0.1337 (0.1302, 0.1372)	0.0763 (0.0728, 0.0798)	0.2308 (0.2273, 0.2343)	0.5201 (0.5170, 0.5232)	0.4801 (0.4790, 0.4808)	0.4811 (0.4772, 0.4847)
Overall	0.3239 (0.3204, 0.3274)	0.3135 (0.3100, 0.3170)	0.2640 (0.2605, 0.2675)	0.3291 (0.3256, 0.3326)	0.3120 (0.3085, 0.3155)	0.4400 (0.4365, 0.4435)	0.5300 (0.5275, 0.5326)	0.5367 (0.5364, 0.5371)	0.6235 (0.6191, 0.6276)

Table A10. Micro-F1 (mean (lower, upper), 95% CI). For single-label classification, Micro-F1 equals accuracy.

Cohort	DINO-B/16	DINO-L/16	DINO-S+/16	LOKI	PLIP	MUSK	Path Local	Path Global	Fusion Gate
Lung	0.6651 (0.6613, 0.6689)	0.6413 (0.6376, 0.6451)	0.3166 (0.3129, 0.3203)	0.7013 (0.6974, 0.7049)	0.4883 (0.4845, 0.4923)	0.6728 (0.6688, 0.6763)	0.8494 (0.8466, 0.8521)	0.8611 (0.8594, 0.8622)	0.8695 (0.8669, 0.8721)
Ovary	0.8153 (0.8134, 0.8173)	0.8213 (0.8193, 0.8233)	0.7048 (0.7025, 0.7071)	0.4973 (0.4948, 0.4998)	0.7713 (0.7692, 0.7735)	0.7266 (0.7244, 0.7290)	0.8910 (0.8894, 0.8924)	0.7452 (0.7446, 0.7463)	0.8932 (0.8916, 0.8949)
Pancreas	0.2451 (0.2427, 0.2478)	0.2521 (0.2495, 0.2546)	0.2131 (0.2105, 0.2157)	0.2199 (0.2174, 0.2223)	0.1587 (0.1566, 0.1609)	0.2615 (0.2589, 0.2643)	0.4967 (0.4937, 0.4998)	0.4722 (0.4703, 0.4733)	0.5003 (0.4973, 0.5036)
Overall	0.5995 (0.5979, 0.6012)	0.6001 (0.5985, 0.6018)	0.4683 (0.4665, 0.4699)	0.4464 (0.4445, 0.4482)	0.5158 (0.5141, 0.5177)	0.5640 (0.5623, 0.5658)	0.7539 (0.7525, 0.7554)	0.7452 (0.7446, 0.7463)	0.7601 (0.7578, 0.7625)

E.1. Does local-aware Gating Benefit the Global Path?

Evaluation Setup We evaluate the effect of the local-aware gating signal specifically on the **Global Path**. All results are computed on the **16-class intersection**.

Finding As shown in Table A11, **local-aware consistently improves Path global** across all metrics:

- Overall accuracy improves by +0.013 and macro F1 by +0.022.
- Calibration is noticeably better: ECE decreases by 0.013 and Brier score decreases by 0.019.
- On challenging subsets, macro F1 increases by +0.026 (low-confidence) and +0.032 (high-entropy).
- AUROC also shows a slight positive change (+0.002).

These results indicate that local-aware gating provides a beneficial confidence prior that stabilizes and strengthens the Global Path’s predictions, even though the mechanism originates from the path local.

Table A11. Effect of local-aware gating on Path global (16-class intersection). Metrics: Acc and macro F1; ECE↓ and Brier↓ (lower is better).

Setting	Acc	F1	ECE↓	Brier↓	AUROC	F1@Low	F1@High
local_aware_ON	0.856	0.773	0.045	0.210	0.990	0.500	0.620
local_aware_OFF	0.842	0.751	0.058	0.229	0.988	0.475	0.589
Δ (ON–OFF)	+0.013	+0.022	-0.013	-0.019	+0.002	+0.026	+0.032

Additional visualizations

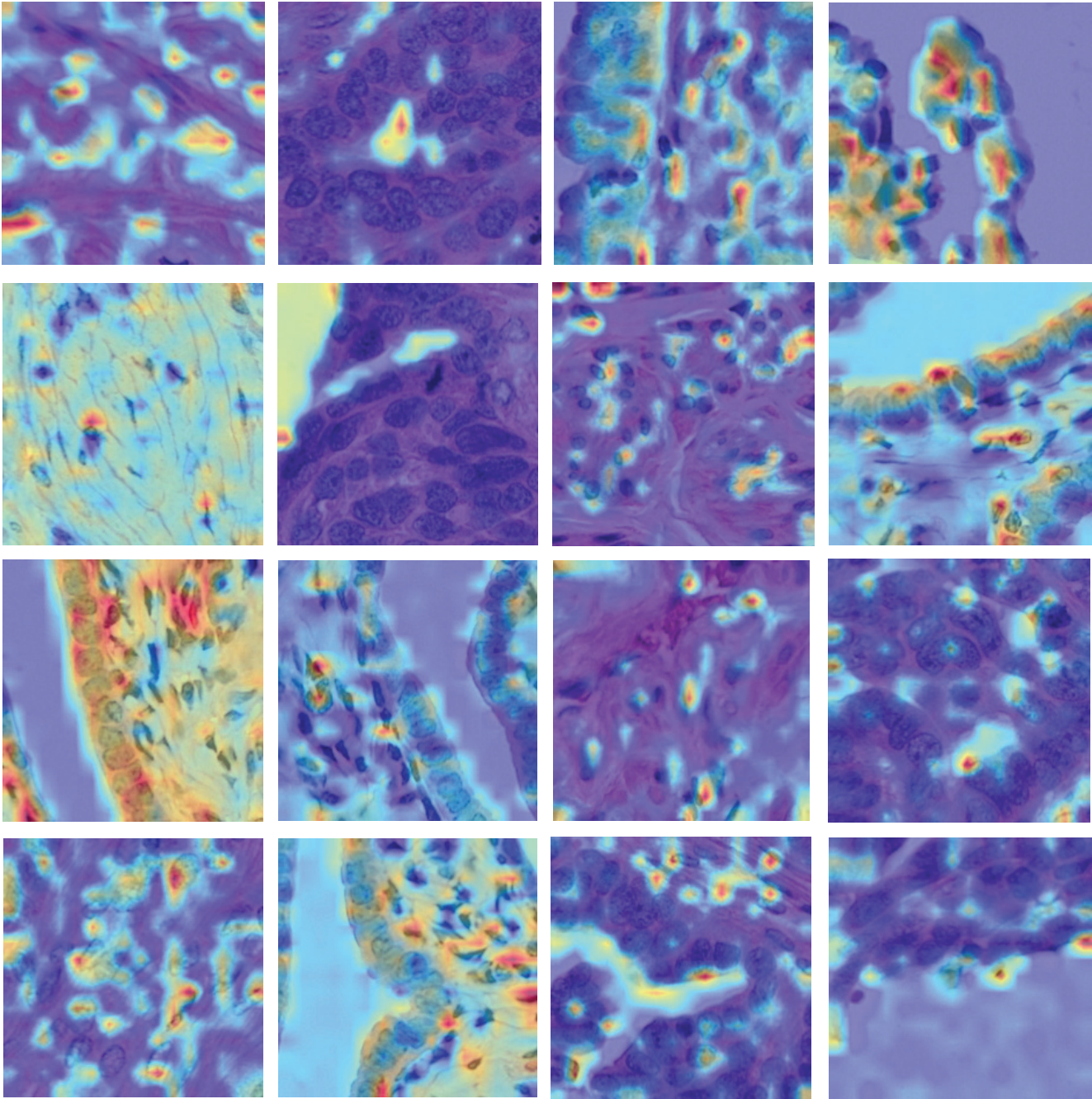
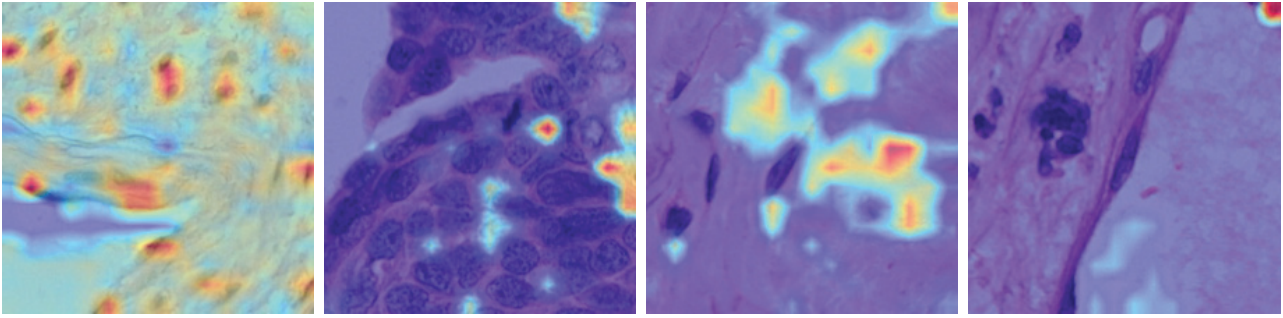
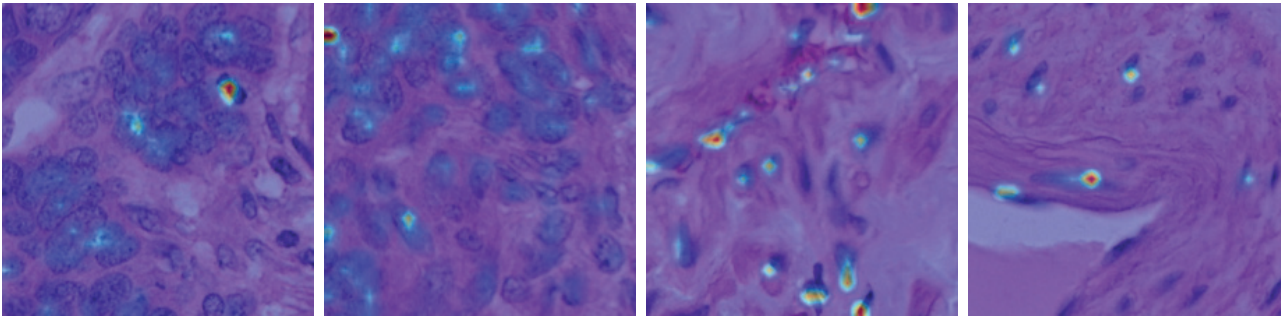


Figure A1. Additional Grad-CAM visualizations (Path-local expert).

Visualization Examples of LOKI on Ovarain Dataset



Visualization Examples of MUSK on Ovarain Dataset



Visualization Examples of PLIP on Ovarain Dataset

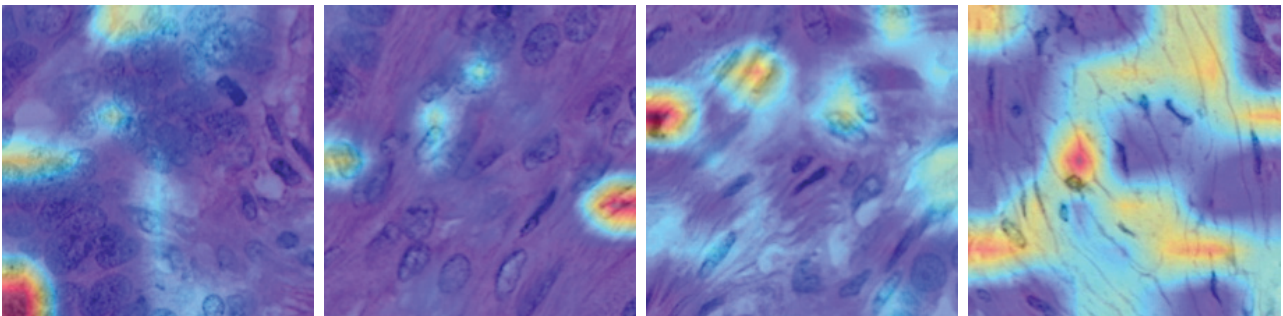


Figure A2. Additional Grad-CAM visualizations for LOKI, MUSK, and PLIP (Ovary).

Acknowledgements

As future work, we plan to evaluate zero-/few-shot transfer on *non-Xenium*, public H&E datasets with coarse label mappings, to further assess cross-panel, cross-stain, and cross-institution generalization. We emphasize that the present study already establishes strong evidence: Xenium provides subcellular-resolution, high-plex spatial gene expression with cell-level coordinates, enabling objective, reproducible labels that serve as a high-quality supervision signal for cell-wise modeling. Our results demonstrate that, under this gold-standard molecular supervision, NuClass succeeds at subcellular granularity and yields calibrated, interpretable predictions across fully held-out cohorts.